



A new 4-node MITC element for analysis of two-dimensional solids and its formulation in a shell element



Yeongbin Ko^a, Phill-Seung Lee^{a,*}, Klaus-Jürgen Bathe^b

^a Department of Mechanical Engineering, Korea Advanced Institute of Science and Technology, 291 Daehak-ro, Yuseong-gu, Daejeon 34141, Republic of Korea

^b Department of Mechanical Engineering, Massachusetts Institute of Technology, Cambridge, MA 02139, USA

ARTICLE INFO

Article history:

Received 19 May 2017

Accepted 3 July 2017

Keywords:

4-node 2D finite element for solids

MITC method

EAS method

Incompatible modes

Shear and volumetric locking

MITC4+ shell element

ABSTRACT

We present in this paper a new reliable and efficient 4-node quadrilateral element, which we call the 2D-MITC4 element, for two-dimensional plane stress and plane strain solutions of solids using the MITC method. We also present an extension of the element assuming a constant element pressure, which we call the 2D-MITC4/1 element. The elements show a much better predictive capability than the displacement-based element and perform in linear analyses almost as well as the 4-node element with incompatible modes, an enhanced assumed strain (EAS) element. However, unlike when using EAS elements, we do not observe spurious instabilities in geometrically nonlinear solutions. Embedding the new MITC formulation into the previously presented MITC4+ shell element, we improve the membrane behavior of the shell element. The new 2D solid elements and the improved MITC4+ shell element pass all basic tests (the isotropy, zero energy mode and patch tests). We present the finite element solutions of various benchmark problems to illustrate the solution accuracy of the new elements.

© 2017 Elsevier Ltd. All rights reserved.

1. Introduction

During the past decades, the development of effective finite elements has been given much focus. Since many continuum problems can be modeled mathematically as two-dimensional (2D) planar problems, 2D solid and fluid elements are frequently used in engineering practice [1–4]. In these analyses, the use of 4-node quadrilateral elements is attractive, but the simple standard 4-node displacement-based element for the analysis of solids suffers from severe loss of accuracy due to in-plane shear and volumetric locking [1,2].

To alleviate the locking behavior of the displacement-based 4-node solid element, incompatible modes have been added [5–7], an approach generalized to the use of 'enhanced assumed strains' (EAS) [3,6]. However, the use of incompatible modes or enhanced strains, can result in spurious instabilities in geometrically nonlinear analyses [4,8–10] and, indeed, even when only small strains are measured [11]. As a remedy, stability factors have been introduced which in engineering practice are not desirable. Also, the EAS elements carry an additional computational expense and in geometrically nonlinear analyses an additional complexity, in that the additional degrees of freedom pertaining to the incompatible

modes or enhanced strains need be processed, usually by static condensation.

The 'mixed interpolation of tensorial components' (MITC) method in which judiciously chosen strain fields are tied to the displacement-based strains has been extensively employed in plate and shell finite element analyses to reduce transverse shear and membrane locking [12–20]. The advantage of this approach is that no additional degrees of freedom are introduced and for well-formulated elements spurious instabilities have not been observed. Also, once a linear formulation for an element has been developed, the extension of the formulation to nonlinear analyses is accomplished as for displacement-based elements [1].

In this paper, we present a new 4-node quadrilateral element for the 2D analyses of solids based on the MITC approach. The new 2D-MITC4 element is based on a new assumed strain field effective to prevent shear locking. To alleviate volumetric locking in the analysis of almost incompressible materials, the assumption of a constant pressure in the element is used [1,21] to obtain the 2D-MITC4/1 element. The new elements provide solution accuracy comparable to the incompatible modes elements and do not show the spurious instabilities seen in incompatible modes elements when used in geometrically nonlinear analyses. The formulation of the new 2D elements is expressed efficiently using physical strain patterns and coefficients inherently used in the formulation of displacement-based elements. Since only the usual displace-

* Corresponding author.

E-mail address: phillseung@kaist.edu (P.S. Lee).

ment degrees of freedom of a 4-node displacement-based element are used, there is no static condensation on internal degrees of freedom and there are no complications in constructing a mass matrix for mode superposition, implicit or explicit dynamic solutions.

Considering shell analyses, the MITC4+ shell element recently proposed provides reliable solutions in linear and nonlinear analyses even when distorted meshes are used [12]. We further improve this shell element by utilizing the assumed strain field of the 2D-MITC4 element for the membrane behavior of the shell element, while keeping the performance in bending and transverse shearing. When used in (planar) 2D plane stress solutions, the shell element gives the same results as the 2D-MITC4 element. We demonstrate the performance of the improved MITC4+ shell element through the solutions of some representative shell problems.

In the following sections, the formulations of the 2D-MITC4 and 2D-MITC4/1 elements and the improved MITC4+ shell element are given. Then basic element tests are considered, and the results of a number of convergence tests are presented. We focus on the accuracy of the solutions obtained, the order of convergence reached, and the stability of the 2D-MITC4 solid element in nonlinear analysis.

2. Formulation of the 2D-MITC4 and 2D-MITC4/1 solid elements

In this section, we present the formulation of the new 2D solid elements based on the MITC method. The treatments of shear locking and volumetric locking are presented.

2.1. Geometry and displacements

The geometry of the standard 4-node quadrilateral 2D solid element is interpolated using [1,3–7]

$$\mathbf{x} = \sum_{i=1}^4 h_i(r, s) \mathbf{x}_i \quad \text{with} \quad \mathbf{x}_i = x_i \mathbf{i}_x + y_i \mathbf{i}_y = [x_i \quad y_i]^T, \quad (1)$$

in which \mathbf{i}_x and \mathbf{i}_y are the unit base vectors of the global Cartesian coordinate system (x, y) , \mathbf{x}_i is the nodal coordinate vector and $h_i(r, s)$ is the two-dimensional interpolation function of the standard isoparametric procedure for node i , see Fig. 1.

We employ the interpolation functions $h_i(r, s)$ in the useful form

$$h_i(r, s) = \frac{1}{4}(1 + \zeta_i r)(1 + \eta_i s) \quad \text{with} \quad i = 1, 2, 3, 4,$$

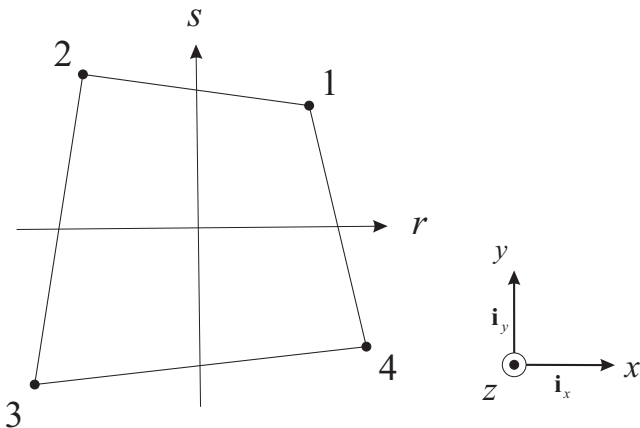


Fig. 1. A standard 4-node quadrilateral 2D solid element.

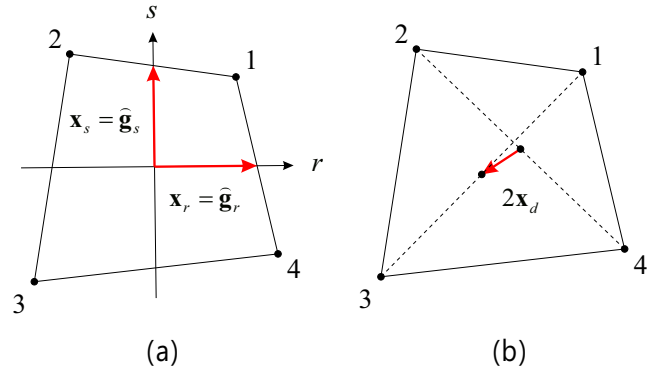


Fig. 2. Representative vectors for the element geometry. (a) Two vectors \mathbf{x}_r and \mathbf{x}_s corresponding to the covariant base vectors at the element center, (b) in-plane distortion vector \mathbf{x}_d .

$$\begin{bmatrix} \zeta_1 & \zeta_2 & \zeta_3 & \zeta_4 \end{bmatrix} = [1 \quad -1 \quad -1 \quad 1], \\ \begin{bmatrix} \eta_1 & \eta_2 & \eta_3 & \eta_4 \end{bmatrix} = [1 \quad 1 \quad -1 \quad -1]. \quad (2)$$

The corresponding displacement interpolation of the element is given as

$$\mathbf{u} = \sum_{i=1}^4 h_i(r, s) \mathbf{u}_i \quad \text{with} \quad \mathbf{u}_i = u_i \mathbf{i}_x + v_i \mathbf{i}_y = [u_i \quad v_i]^T, \quad (3)$$

in which \mathbf{u}_i is the nodal displacement vector in the global Cartesian coordinate system at node i .

The covariant base vectors and displacement derivatives for the 2D solid element are expressed as

$$\begin{aligned} \mathbf{g}_r &= \frac{\partial \mathbf{x}}{\partial r} = \mathbf{x}_r + s \mathbf{x}_d, & \mathbf{u}_r &= \frac{\partial \mathbf{u}}{\partial r} = \mathbf{u}_r + s \mathbf{u}_d, \\ \mathbf{g}_s &= \frac{\partial \mathbf{x}}{\partial s} = \mathbf{x}_s + r \mathbf{x}_d, & \mathbf{u}_s &= \frac{\partial \mathbf{u}}{\partial s} = \mathbf{u}_s + r \mathbf{u}_d, \end{aligned} \quad (4)$$

with the following characteristic geometry and displacement vectors

$$\begin{aligned} \mathbf{x}_r &= \frac{1}{4} \sum_{i=1}^4 \zeta_i \mathbf{x}_i, & \mathbf{x}_s &= \frac{1}{4} \sum_{i=1}^4 \eta_i \mathbf{x}_i, & \mathbf{x}_d &= \frac{1}{4} \sum_{i=1}^4 \zeta_i \eta_i \mathbf{x}_i, \\ \mathbf{u}_r &= \frac{1}{4} \sum_{i=1}^4 \zeta_i \mathbf{u}_i, & \mathbf{u}_s &= \frac{1}{4} \sum_{i=1}^4 \eta_i \mathbf{u}_i, & \mathbf{u}_d &= \frac{1}{4} \sum_{i=1}^4 \zeta_i \eta_i \mathbf{u}_i, \end{aligned} \quad (5)$$

where the vectors \mathbf{x}_r , \mathbf{x}_s and \mathbf{x}_d shown in Fig. 2 arise naturally from the element geometry.

In Eq. (4), the two vectors \mathbf{x}_r and \mathbf{x}_s are the covariant base vectors at the element center,

$$\mathbf{x}_r = \widehat{\mathbf{g}}_r = \mathbf{g}_r(0, 0), \quad \mathbf{x}_s = \widehat{\mathbf{g}}_s = \mathbf{g}_s(0, 0), \quad (6)$$

and the vector \mathbf{x}_d is only non-zero when the element geometry is distorted. Note that the three vectors \mathbf{x}_r , \mathbf{x}_s and \mathbf{x}_d are completely independent of each other and fully represent the characteristics of the planar geometry of the quadrilateral element.

The contravariant base vectors \mathbf{g}^j are defined using the covariant base vectors in Eq. (4)

$$\mathbf{g}_i \cdot \mathbf{g}^j = \delta_i^j \quad \text{with} \quad \mathbf{g}_1 = \mathbf{g}_r, \quad \mathbf{g}_2 = \mathbf{g}_s, \quad \mathbf{g}^1 = \mathbf{g}^r, \quad \mathbf{g}^2 = \mathbf{g}^s, \quad (7)$$

and the strain tensor (\mathbf{e}) and its covariant components (e_{ij}) are

$$\mathbf{e} = e_{ij}(\mathbf{g}^i \otimes \mathbf{g}^j) \quad \text{with} \quad e_{ij} = \frac{1}{2}(\mathbf{g}_i \cdot \mathbf{u}_j + \mathbf{g}_j \cdot \mathbf{u}_i). \quad (8)$$

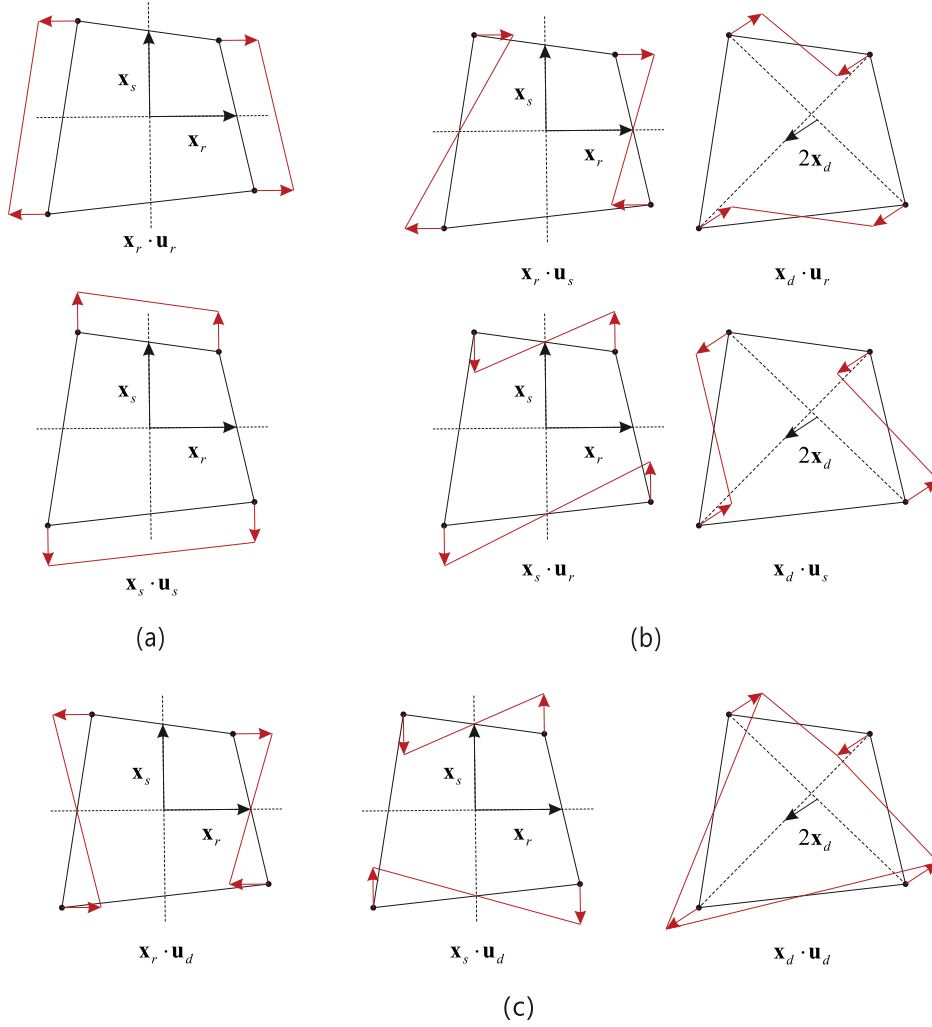


Fig. 3. Physical strain patterns from the characteristic geometry and displacements. (a) Stretching strains. (b) Shearing strains. (c) Bending strains.

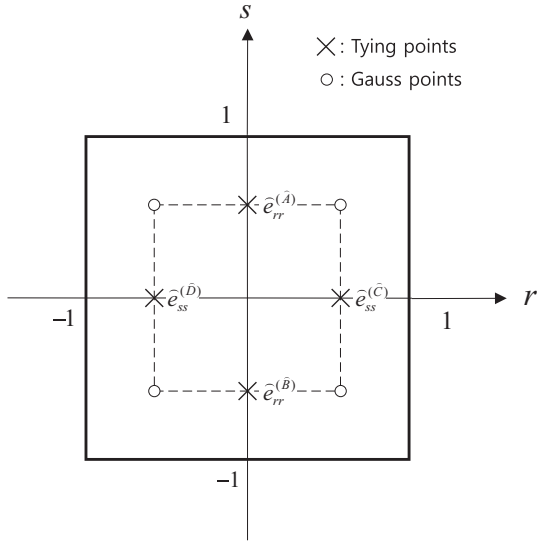


Fig. 4. Tying positions and corresponding strain components for the assumed strain of the 2D-MITC4 element.

in which $\mathbf{g}_i = \frac{\partial \mathbf{x}}{\partial r_i}$ and $\mathbf{u}_i = \frac{\partial \mathbf{u}}{\partial r_i}$ with $r_1 = r$, $r_2 = s$. Note that $e_{11} = e_{rr}$, $e_{22} = e_{ss}$ and $e_{12} = e_{rs}$.

The covariant strain components can be obtained using the characteristic geometry and displacement vectors [12]

$$\begin{aligned} e_{rr} &= e_{rr}|_{con} + e_{rr}|_{lin} \cdot s + e_{rs}|_{bil} \cdot s^2, \\ e_{ss} &= e_{ss}|_{con} + e_{ss}|_{lin} \cdot r + e_{rs}|_{bil} \cdot r^2, \end{aligned} \quad (9)$$

$$e_{rs} = e_{rs}|_{con} + \frac{1}{2} e_{rr}|_{lin} \cdot r + \frac{1}{2} e_{ss}|_{lin} \cdot s + e_{rs}|_{bil} \cdot rs,$$

with

$$\begin{aligned} e_{rr}|_{con} &= \mathbf{x}_r \cdot \mathbf{u}_r, & e_{ss}|_{con} &= \mathbf{x}_s \cdot \mathbf{u}_s, & e_{rs}|_{con} &= \frac{1}{2} (\mathbf{x}_r \cdot \mathbf{u}_s + \mathbf{x}_s \cdot \mathbf{u}_r), \\ e_{rr}|_{lin} &= \mathbf{x}_r \cdot \mathbf{u}_d + \mathbf{x}_d \cdot \mathbf{u}_r, & e_{ss}|_{lin} &= \mathbf{x}_s \cdot \mathbf{u}_d + \mathbf{x}_d \cdot \mathbf{u}_s, & e_{rs}|_{bil} &= \mathbf{x}_d \cdot \mathbf{u}_d, \end{aligned} \quad (10)$$

in which 'con', 'lin' and 'bil' denote constant, linear and bilinear terms, respectively.

We refer to the strain coefficients in Eq. (10) as 'physical strain coefficients' because they correspond to the physical strain patterns of stretching, bending and shearing in the directions of \mathbf{x}_r , \mathbf{x}_s and \mathbf{x}_d as shown in Fig. 3. We will establish a new combination of these physical strain patterns, to pass the patch tests and obtain an improved element membrane behavior.

2.2. New assumed strain field

To establish the strain field of the new 2D-MITC4 element (and the 2D-MITC4/1 element), we use instead of the covariant strain components in Eq. (9) the following strain components

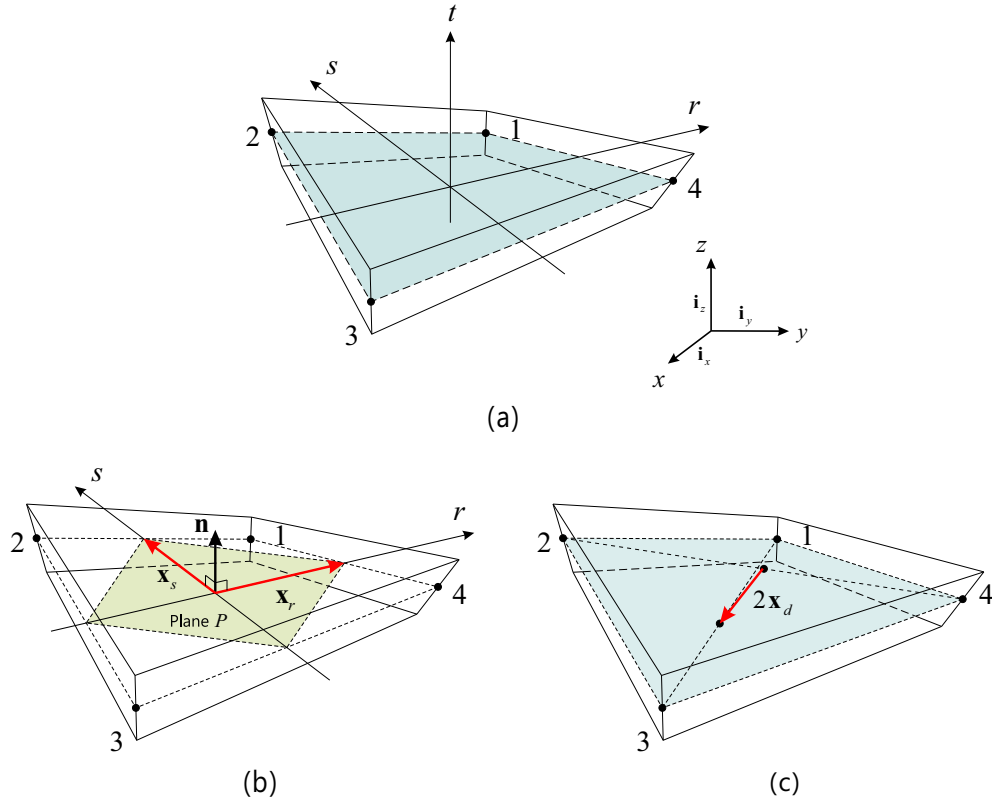


Fig. 5. Mid-surface geometry and representative vectors for the shell element. (a) Geometry of shell mid-surface (colored). (b) Two in-plane vectors \mathbf{x}_r and \mathbf{x}_s in the plane P with normal vector \mathbf{n} . (c) 3D distortion vector \mathbf{x}_d . (For interpretation of the references to colour in this figure legend, the reader is referred to the web version of this article.)

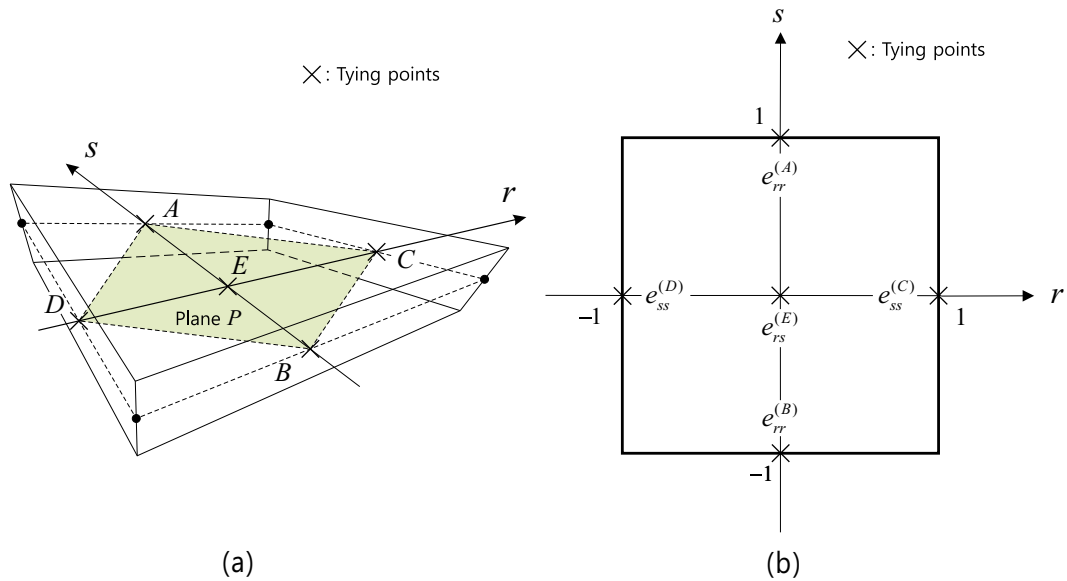


Fig. 6. Tying positions for the assumed membrane strain of the improved MITC4+ element. (a) Tying positions in 3D space. (b) Tying positions in (r, s) space and corresponding strains.

$$\hat{e}_{ij} = e_{kl} g_i^k g_j^l \quad \text{with} \quad g_i^j = \hat{\mathbf{g}}_i \cdot \mathbf{g}^j \quad \text{and} \quad \hat{\mathbf{g}}_i = \mathbf{g}_i(0, 0), \quad (11)$$

in which $\hat{\mathbf{g}}_i$ is the covariant base vector evaluated at the element center. Using these strain components to establish the strain field is beneficial for passing the patch tests [3,6,22].

The new assumed strain field is

$$\begin{aligned} \hat{e}_{rr} &= e_{rr}(0, 0) + \frac{\sqrt{3}}{2} \lambda(r, s) (\hat{e}_{rr}^{(A)} - \hat{e}_{rr}^{(B)}) s, \\ \hat{e}_{ss} &= e_{ss}(0, 0) + \frac{\sqrt{3}}{2} \lambda(r, s) (\hat{e}_{ss}^{(C)} - \hat{e}_{ss}^{(D)}) r, \\ \hat{e}_{rs} &= e_{rs}(0, 0), \end{aligned} \quad (12)$$

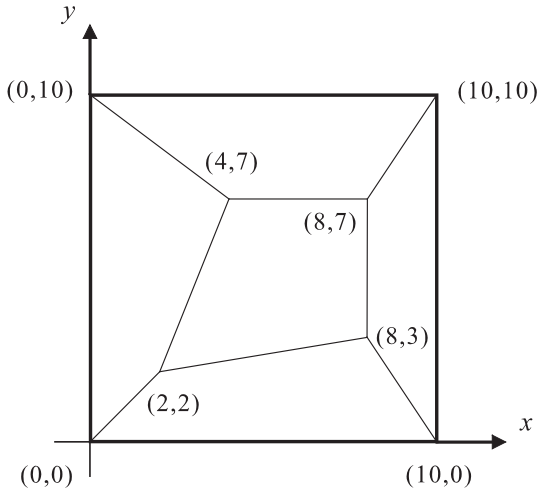


Fig. 7. Patch of elements used for the patch tests.

where the tying points (\hat{A}) , (\hat{B}) , (\hat{C}) and (\hat{D}) are shown in Fig. 4 and $\lambda(r,s)$ is the ratio of the determinants of the Jacobian matrices

$$\lambda(r,s) = \frac{j(0,0)}{j(r,s)} \quad \text{with} \quad j(r,s) = \det[\mathbf{g}_r \quad \mathbf{g}_s]. \quad (13)$$

We use $\lambda(r,s)$ in Eq. (12) to have the element pass the patch tests. While using the strain components evaluated at the element center to represent constant strain behaviors, the linear terms in Eq. (12) are employed to obtain the correct rank and good bending behavior. The assumed strain fields in Eq. (12) are closely related to the fields of the QMITC element proposed by Dvorkin and Vassolo [22]. However, we use only the 4 element corner nodes to interpolate the displacements and interpolate the normal strain components differently to obtain a simpler field that improves the membrane behavior, see Refs. [23,24].

In order to reduce the computational cost, the assumed strain components in Eq. (12) can be directly obtained using the covariant strain terms in Eq. (9) without recourse to the strain transformation in Eq. (11). Namely, the assumed strain field is given as a linear combination of the physical strain patterns

$$\begin{aligned} \hat{e}_{rr} &= e_{rr}|_{con} + \lambda(r,s) \hat{e}_{rr}^{lin} s, \\ \hat{e}_{ss} &= e_{ss}|_{con} + \lambda(r,s) \hat{e}_{ss}^{lin} r, \\ \hat{e}_{rs} &= e_{rs}|_{con}, \end{aligned} \quad (14)$$

Table 1

Predicted vertical displacement at the tip (point A) in the cantilever problem.

Elements	Regular mesh	Distorted mesh
Q4	0.235608	0.203966
Q4I4	0.347810	0.342552
2D-MITC4, 2D-MITC4/1	0.347810	0.302102
Exact solution	0.347810	

Table 2

Predicted stress-xx ($\times 10^2$) at the support (point B) in the cantilever problem.

Elements	Regular mesh	Distorted mesh
Q4	0.466667	0.351417
Q4I4	0.700000	0.615516
2D-MITC4, 2D-MITC4/1	0.700000	0.580764
Exact solution	0.700000	

with

$$\begin{aligned} \hat{e}_{rr}^{lin} &= \left(\frac{n_1}{\sqrt{3}} e_{rs}|_{bil} + \sqrt{3} n_1 e_{rr}|_{con} + \sqrt{3} n_2 e_{ss}|_{con} + n_3 e_{rr}|_{lin} + n_4 e_{ss}|_{lin} + 2\sqrt{3} n_5 e_{rs}|_{con} \right), \\ \hat{e}_{ss}^{lin} &= \left(\frac{m_1}{\sqrt{3}} e_{rs}|_{bil} + \sqrt{3} m_1 e_{ss}|_{con} + \sqrt{3} m_2 e_{rr}|_{con} + m_3 e_{ss}|_{lin} + m_4 e_{rr}|_{lin} + 2\sqrt{3} m_5 e_{rs}|_{con} \right), \\ n_1 &= \frac{1}{2} [(g_r^r|_{\hat{A}})^2 - (g_r^r|_{\hat{B}})^2], \quad n_2 = \frac{1}{2} [(g_s^s|_{\hat{A}})^2 - (g_s^s|_{\hat{B}})^2], \\ n_3 &= \frac{1}{2} [(g_r^r|_{\hat{A}})^2 + (g_r^r|_{\hat{B}})^2], \quad n_4 = \frac{1}{2} [g_r^r|_{\hat{A}} \cdot g_r^s|_{\hat{A}} + g_r^r|_{\hat{B}} \cdot g_r^s|_{\hat{B}}], \\ n_5 &= \frac{1}{2} [g_r^r|_{\hat{A}} \cdot g_r^s|_{\hat{A}} - g_r^r|_{\hat{B}} \cdot g_r^s|_{\hat{B}}], \\ m_1 &= \frac{1}{2} [(g_s^s|_{\hat{C}})^2 - (g_s^s|_{\hat{D}})^2], \quad m_2 = \frac{1}{2} [(g_r^r|_{\hat{C}})^2 - (g_r^r|_{\hat{D}})^2], \\ m_3 &= \frac{1}{2} [(g_s^s|_{\hat{C}})^2 + (g_s^s|_{\hat{D}})^2], \quad m_4 = \frac{1}{2} [g_r^r|_{\hat{C}} \cdot g_s^s|_{\hat{C}} + g_r^r|_{\hat{D}} \cdot g_s^s|_{\hat{D}}], \\ m_5 &= \frac{1}{2} [g_r^r|_{\hat{C}} \cdot g_s^s|_{\hat{C}} - g_r^r|_{\hat{D}} \cdot g_s^s|_{\hat{D}}], \end{aligned} \quad (15)$$

in which $g_i^j|_{(\cdot)}$ is g_i^j evaluated at a tying point (\cdot) . Note that in Eq. (14) the strain terms $e_{ij}|_{con}$, \hat{e}_{rr}^{lin} and \hat{e}_{ss}^{lin} are constant within the element (hence are only evaluated once during the numerical integration).

2.3. Treatment of volumetric locking, the 2D-MITC4/1 element

When the above formulated 2D-MITC4 element is used in plane strain analysis of almost incompressible materials, volumetric

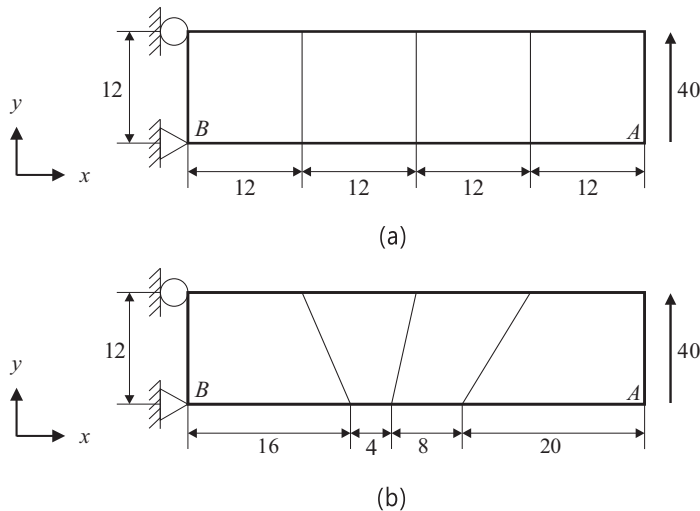


Fig. 8. Cantilever problem (plane stress conditions, 1×4 mesh, $E = 3.0 \times 10^4$ and $\nu = 0.0$). (a) Regular mesh. (b) Distorted mesh.

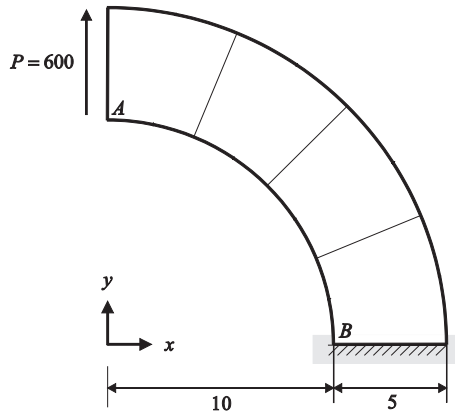


Fig. 9. Curved beam problem (plane stress conditions, 1×4 mesh, $E = 1.0 \times 10^3$ and $\nu = 0.0$).

Table 3
Predicted vertical displacement at the tip (point A) in the curved beam problem.

Elements	Regular mesh			
	1×4	2×8	4×16	8×32
Q4	57.9325	79.1450	87.2312	89.5583
Q4I4	84.6070	88.2500	89.7753	90.2226
2D-MITC4, 2D-MITC4/1	82.4881	88.0888	89.7646	90.2219
Reference solution	90.4100			

Table 4
Predicted stress-yy ($\times 10^3$) at the support (point B) in the curved beam problem.

Elements	Regular mesh			
	1×4	2×8	4×16	8×32
Q4	1.65873	2.01208	2.09773	2.05927
Q4I4	2.45257	2.26952	2.15383	2.06920
2D-MITC4, 2D-MITC4/1	1.99949	2.15453	2.13429	2.06343
Reference solution	2.03932			

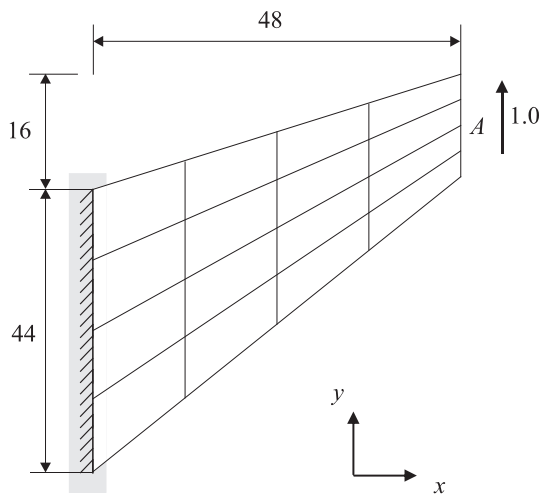


Fig. 10. Cook's problem (4×4 mesh, $E = 1.0$, plane stress conditions with $\nu = 1/3$; plane strain conditions with $\nu = 0.3$, $\nu = 0.4$ or $\nu = 0.499$).

locking can occur. To alleviate volumetric locking, we use the u/p formulation with the assumption of constant element pressure, although the element then does not pass the inf-sup condition [1,2]. The undesirable consequence is that for certain meshes and boundary conditions, pressure checker-boarding can be present.

Table 5

Predicted vertical displacement at point A in Cook's problem with plane stress conditions.

Elements	Mesh				
	2×2	4×4	8×8	16×16	32×32
Q4	11.8452	18.2992	22.0792	23.4304	23.8176
Q4I4	21.0503	23.0164	23.6888	23.8833	23.9398
2D-MITC4	17.4146	21.8089	23.3378	23.7894	23.9145
2D-MITC4/1	19.6105	22.6393	23.5860	23.8572	23.9334
Reference solution	23.9642				

In practice, the meshes used frequently do not allow pressure checker-boarding and if it occurs, the phenomenon is seen when plotting the pressure. For computational efficiency we do not introduce an additional pressure variable but simply employ a constant volumetric strain [1,21] in the element. The use of the constant volumetric strain can also improve the behavior of the plane stress element.

The strain components in Eqs. (9) and (14) are transformed into the global Cartesian coordinates,

$$\bar{\epsilon}_{ij}^{st} = e_{kl}(\mathbf{i}_i \cdot \mathbf{g}^k)(\mathbf{j}_j \cdot \mathbf{g}^l), \quad \bar{\epsilon}_{ij}^{as} = \hat{e}_{kl}(\mathbf{i}_i \cdot \mathbf{g}^k)(\mathbf{j}_j \cdot \mathbf{g}^l) \quad \text{with} \quad \mathbf{i}_1 = \mathbf{i}_x, \quad \mathbf{i}_2 = \mathbf{i}_y, \quad (16)$$

in which \mathbf{g}^k is the contravariant base vector evaluated at the element center, and the superscripts 'st' and 'as' denote the standard displacement based and assumed strain components, respectively.

The volumetric strain is assumed to be constant within the element and is obtained from the strain components evaluated at the element center

$$\bar{\epsilon}^{vol} = \bar{\epsilon}_{xx}^{st}(0,0) + \bar{\epsilon}_{yy}^{st}(0,0) = \bar{\mathbf{B}}^{vol} \mathbf{U} \quad \text{with} \quad \mathbf{U} = [\mathbf{u}_1 \quad \mathbf{u}_2 \quad \mathbf{u}_3 \quad \mathbf{u}_4]^T. \quad (17)$$

and the deviatoric strain components are obtained from

$$\bar{\epsilon}_{ij}^{dev} = \bar{\epsilon}_{ij}^{as} - \frac{1}{2} \bar{\epsilon}^{vol} \delta_{ij} = \bar{\mathbf{B}}_{ij}^{dev} \mathbf{U}. \quad (18)$$

The stiffness matrix of the 2D-MITC4/1 element is then given by

$$\mathbf{K} = \int_{V_e} (\kappa + \frac{\mu}{3} G) \bar{\mathbf{B}}^{volT} \bar{\mathbf{B}}^{vol} dV_e + \int_{V_e} \bar{\mathbf{B}}_{ij}^{devT} \mathbf{C}_{ij}^{dev} \bar{\mathbf{B}}_{ij}^{dev} dV_e, \quad (19)$$

in which V_e is the element volume, $\mu = \frac{(1-4\nu)(1+\nu)}{(1-2\nu)(1-\nu)}$ and $\mu = 1$ for the plane stress and plane strain cases, respectively, the bulk modulus $\kappa = \frac{E}{3(1-2\nu)}$ and the shear modulus $G = \frac{E}{2(1+\nu)}$ with Young's modulus E and Poisson's ratio ν , and \mathbf{C}_{ij}^{dev} is the material law tensor for the deviatoric strain and stress ($C_{11}^{dev} = C_{22}^{dev} = 2G$ and $C_{12}^{dev} = G$).

Note that Eq. (19) provides a unified formulation of the 2D-MITC4/1 element for plane stress and plane strain analyses, in which volumetric locking for the plane strain case is alleviated. For plane strain analyses with any Poisson's ratio we may use the 2D-MITC4/1 element, but for plane stress analyses we can use the 2D-MITC4 element or the 2D-MITC4/1 element. We show in Sections 5.1–5.3 the differences in results obtained using the two elements.

For the shell element, we do not use the assumption of constant pressure and when using the element in (planar) plane stress problems, the same results as given by the 2D-MITC4 element are obtained.

3. Application to the MITC4+ shell element

In this section we improve the MITC4+ shell element, in which the assumed membrane strain field of the 2D-MITC4 solid element

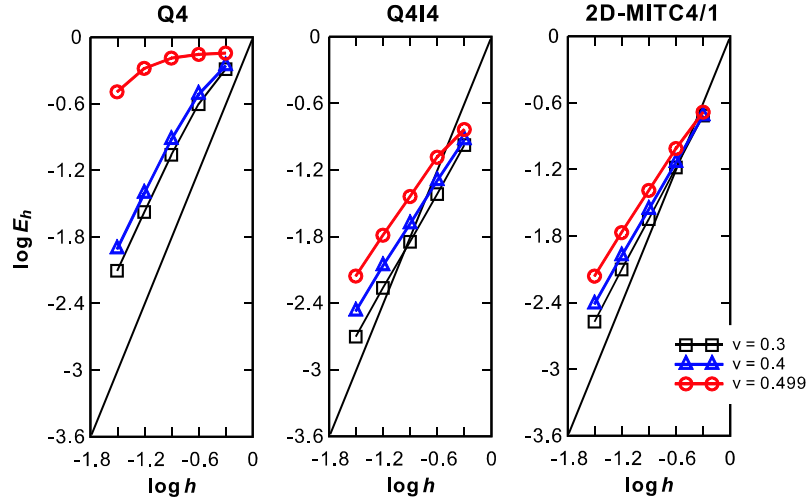


Fig. 11. Convergence curves for Cook's problem with plane strain conditions. The bold line represents the optimal convergence rate.

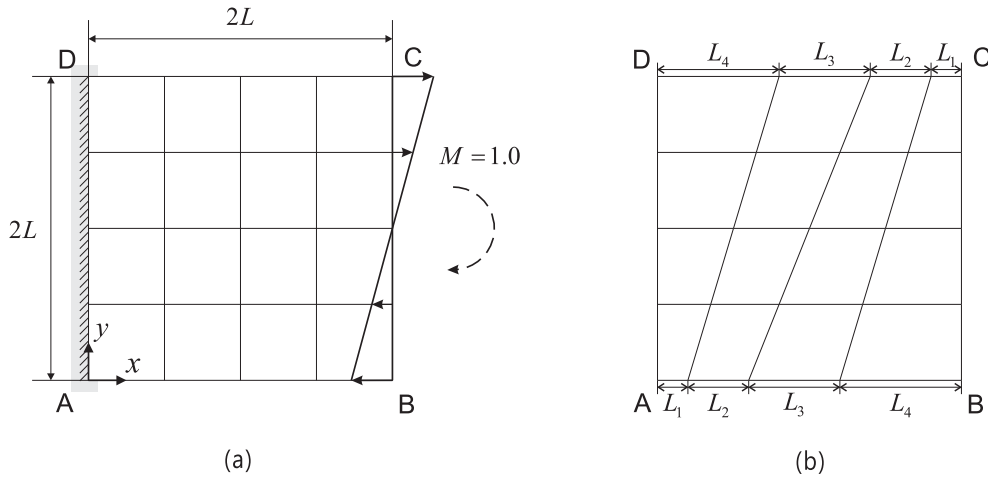


Fig. 12. Clamped square plate subjected to in-plane moment (plane strain conditions, $L = 1.0$, $E = 1.0$, $M = 1.0$, and $\nu = 0.3, 0.4$ or 0.499). (a) Problem description with regular mesh (4×4 mesh). (b) Distorted mesh (4×4 mesh).

formulated in Section 2 is applied. The strains in continuum-mechanics based shell elements can be identified as membrane, bending and transverse shear strains [12]. We focus here only on the formulation and improvement of the membrane strain. Following the MITC approach, the assumed membrane strain components are tied to the displacement-based strain components to ensure computational efficiency.

In the formulation we use Eq. (14) in the compact form

$$\begin{bmatrix} \hat{e}_{rr} \\ \hat{e}_{ss} \end{bmatrix} = \mathbf{M}(r, s)^T [e_{rr|con} \quad e_{ss|con} \quad e_{rs|con} \quad e_{rr|lin} \quad e_{ss|lin} \quad e_{rs|bil}]^T, \quad (20a)$$

$$\hat{e}_{rs} = e_{rs|con},$$

where

$$\mathbf{M}(r, s) = \lambda \begin{bmatrix} 1/\lambda + \sqrt{3}n_1s & \sqrt{3}m_2r \\ \sqrt{3}n_2s & 1/\lambda + \sqrt{3}m_1r \\ 2\sqrt{3}n_5s & 2\sqrt{3}m_5r \\ n_3s & m_4r \\ n_4s & m_3r \\ n_1s/\sqrt{3} & m_1r/\sqrt{3} \end{bmatrix}. \quad (20b)$$

The mid-surface geometry of the 4-node continuum mechanics based shell element is interpolated using [1,12,19]

$$\mathbf{x} = \sum_{i=1}^4 h_i(r, s) \mathbf{x}_i, \quad (21a)$$

$$\mathbf{x}_i = x_i \mathbf{i}_x + y_i \mathbf{i}_y + z_i \mathbf{i}_z = [x_i \quad y_i \quad z_i]^T, \quad (21b)$$

in which \mathbf{i}_x , \mathbf{i}_y and \mathbf{i}_z are the unit base vectors for the global Cartesian coordinates (x, y, z) , and \mathbf{x}_i is the nodal position vector of node i , see Fig. 5(a).

The displacements are interpolated correspondingly

$$\mathbf{u} = \sum_{i=1}^4 h_i(r, s) \mathbf{u}_i, \quad (22a)$$

$$\mathbf{u}_i = u_i \mathbf{i}_x + v_i \mathbf{i}_y + w_i \mathbf{i}_z = [u_i \quad v_i \quad w_i]^T, \quad (22b)$$

in which \mathbf{u}_i is the nodal displacement vector at node i .

Using the interpolations in Eqs. (21) and (22), the characteristic vectors in Eq. (5) as well as the physical strain coefficients in Eq. (10) are defined for the mid-surface of the shell element [12].

Using Eqs. (21) and (22) in Eqs. (4) and (5), the two mid-surface covariant base vectors \mathbf{g}_r and \mathbf{g}_s are evaluated, and the third covari-

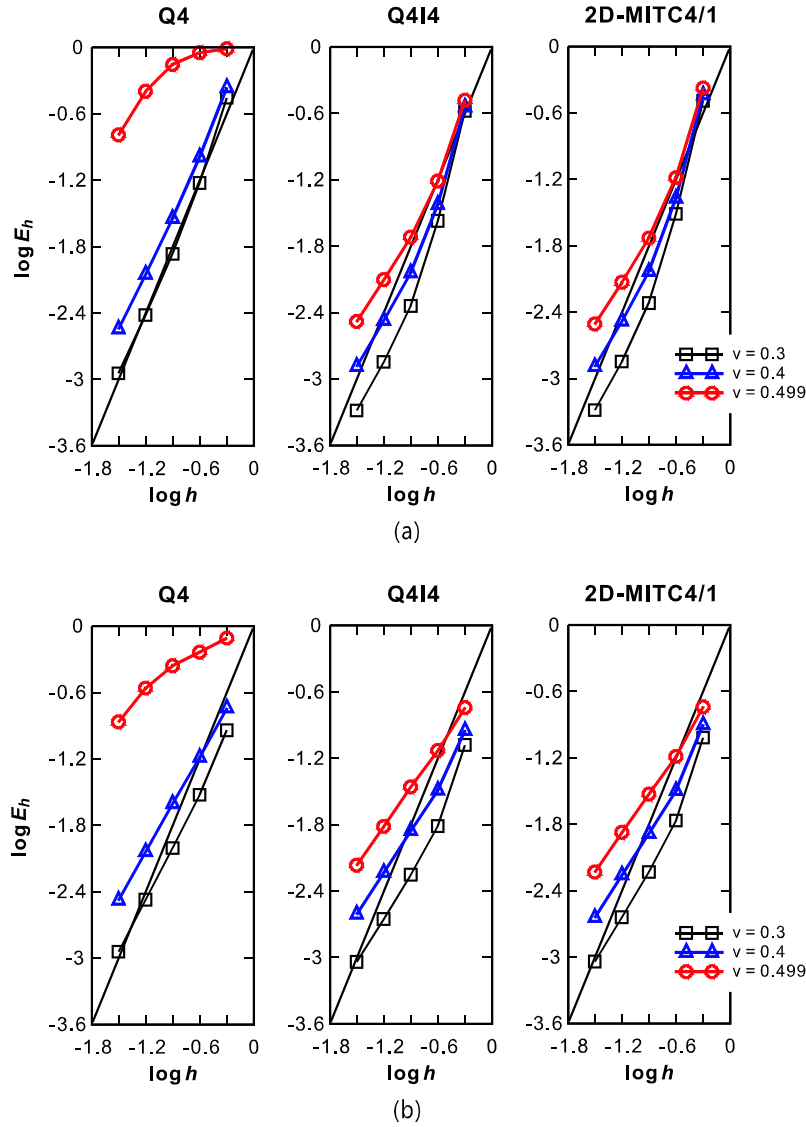


Fig. 13. Convergence curves for the clamped square plate subjected to in-plane moment using (a) the uniform meshes and (b) distorted meshes. The bold line represents the optimal convergence rate.

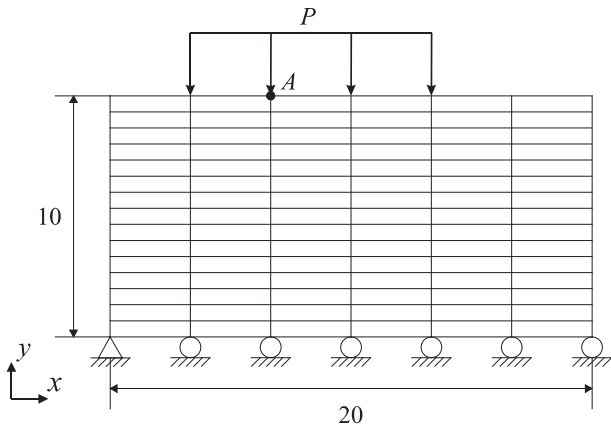


Fig. 14. Rubber block problem (15×6 element mesh, plane strain conditions, $E = 1.0 \times 10^3$ and $\nu = 0.49$).

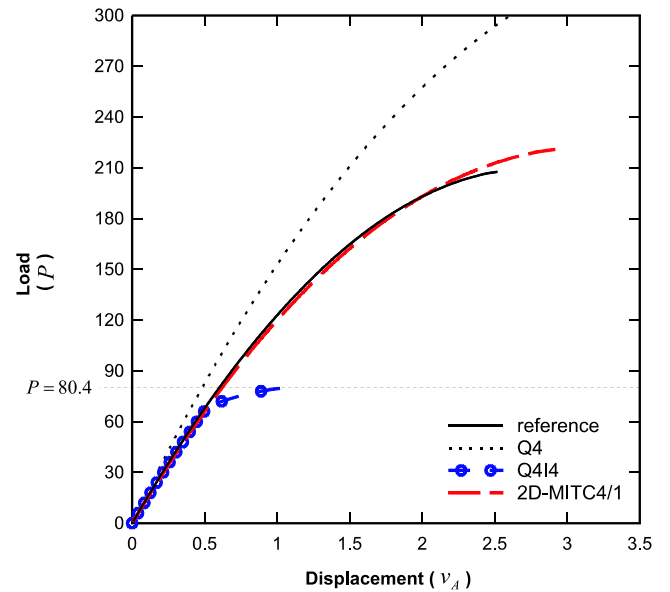


Fig. 15. Predicted load-displacement curves for the rubber block.

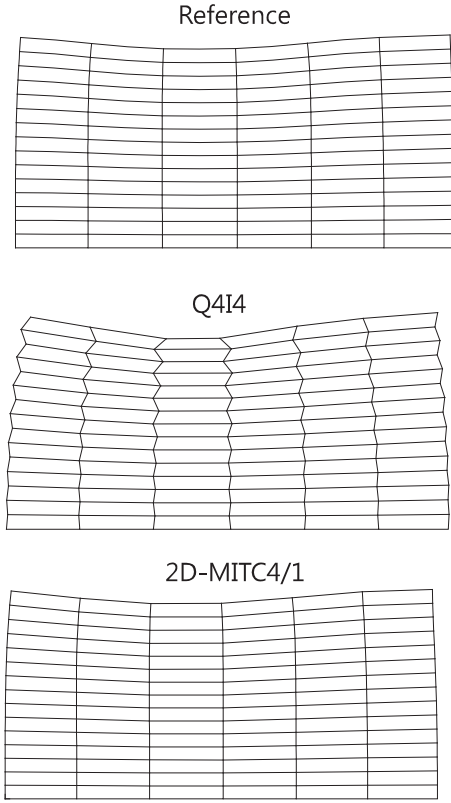


Fig. 16. Deformed shapes (drawn to scale) of the rubber block at $P = 80.4$.

ant and contravariant base vectors are established at the center of the shell mid-surface

$$\mathbf{g}_3 = \mathbf{g}^3 = \widehat{\mathbf{g}}_3 = \widehat{\mathbf{g}}^3 = \mathbf{n} \quad \text{with} \quad \mathbf{n} = \frac{\mathbf{x}_r \times \mathbf{x}_s}{|\mathbf{x}_r \times \mathbf{x}_s|}, \quad (23)$$

in which the vector \mathbf{n} is normal to the flat plane P formed by the characteristic geometry vectors \mathbf{x}_r and \mathbf{x}_s , see Fig. 5(b).

In the shell element, the vector \mathbf{x}_d denotes both in-plane and out-of-plane geometric distortions, see Fig. 5(c). We use the base vectors defined using Eqs. (5) and (23) to calculate the coefficients g_i^j in Eq. (11) for the shell element. The volume ratio λ in Eq. (13) for the shell element is calculated using $j(r, s) = \det[\mathbf{g}_r \quad \mathbf{g}_s \quad \mathbf{n}]$.

To obtain the improved membrane strain, we embed the assumed membrane strain of the 2D-MITC4 element as used for flat mid-surface geometries, while the other assumptions of the

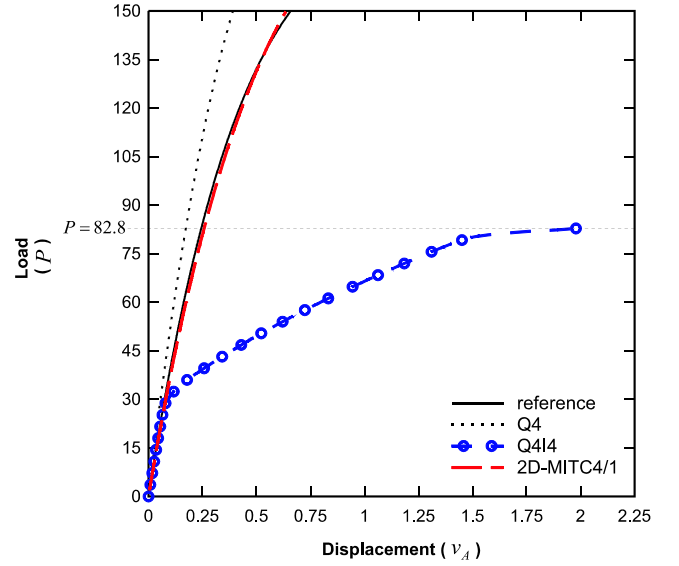


Fig. 18. Load-displacement curves for the composite block problem.

MITC4+ shell element are employed to also avoid membrane locking due to the in-plane and out-of-plane distortions.

The strains sampled at the five tying points in Fig. 6 are related to the physical strain coefficients as follows:

$$\begin{aligned} e_{rs}|_{bil} + e_{rr}|_{con} &= \frac{1}{2}(e_{rr}^{(A)} + e_{rr}^{(B)}), & e_{rr}|_{lin} &= \frac{1}{2}(e_{rr}^{(A)} - e_{rr}^{(B)}), \\ e_{rs}|_{bil} + e_{ss}|_{con} &= \frac{1}{2}(e_{ss}^{(C)} + e_{ss}^{(D)}), & e_{ss}|_{lin} &= \frac{1}{2}(e_{ss}^{(C)} - e_{ss}^{(D)}), \\ e_{rs}|_{con} &= e_{rs}^{(E)}. \end{aligned} \quad (24)$$

Using Eq. (24) in Eq. (14), the assumed membrane strain field can be expressed in terms of $e_{rr}^{(A)}$, $e_{rr}^{(B)}$, $e_{ss}^{(C)}$, $e_{ss}^{(D)}$, $e_{rs}^{(E)}$ and $e_{rs}|_{bil}$. We then substitute the following assumed strain for the strain component $e_{rs}|_{bil}$ [12],

$$\tilde{e}_{rs}|_{bil} = a_A e_{rr}^{(A)} + a_B e_{rr}^{(B)} + a_C e_{ss}^{(C)} + a_D e_{ss}^{(D)} + a_E e_{rs}^{(E)} \quad (25)$$

with

$$\begin{aligned} a_A &= \frac{c_r(c_r - 1)}{2d}, & a_B &= \frac{c_r(c_r + 1)}{2d}, & a_C &= \frac{c_s(c_s - 1)}{2d}, \\ a_D &= \frac{c_s(c_s + 1)}{2d}, & a_E &= \frac{2c_r c_s}{d}, \end{aligned}$$

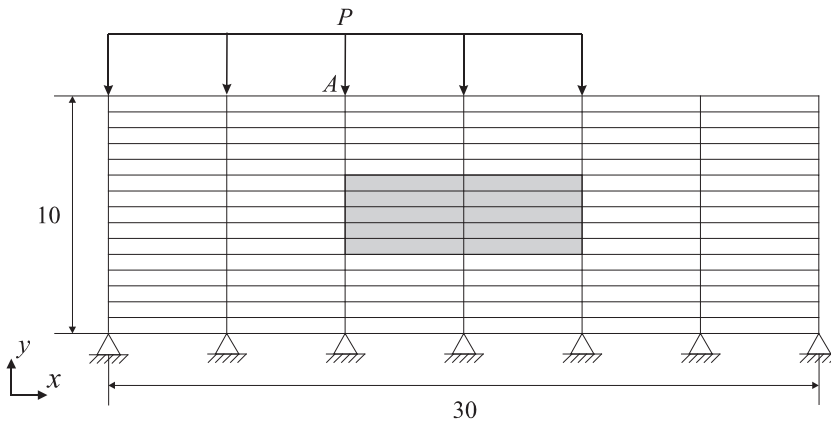


Fig. 17. Composite block problem (15×6 mesh, plane strain conditions, $E = 1.0 \times 10^3$ and $\nu = 0.49$ in non-shaded region and $E = 1.0 \times 10^6$ and $\nu = 0.3$ in shaded region).

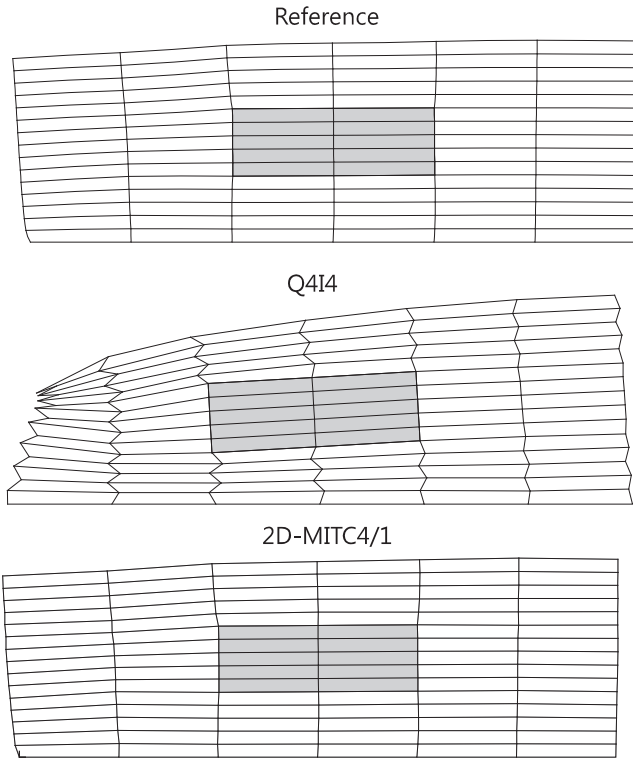


Fig. 19. Deformed shapes (drawn to scale) of the composite block at $P = 82.8$.

$$c_r = \mathbf{x}_d \cdot \hat{\mathbf{g}}^r, \quad c_s = \mathbf{x}_d \cdot \hat{\mathbf{g}}^s, \quad d = c_r^2 + c_s^2 - 1,$$

which produces $e_{rs|bil}$ in flat geometries but alleviates membrane locking in case curved geometries are considered.

Eqs. (24) and (25) can be written as

$$[e_{rr|con} \quad e_{ss|con} \quad e_{rs|con} \quad e_{rr|lin} \quad e_{ss|lin} \quad \tilde{e}_{rs|bil}]^T = \mathbf{C} [e_{rr}^{(A)} \quad e_{rr}^{(B)} \quad e_{ss}^{(C)} \quad e_{ss}^{(D)} \quad e_{rs}^{(E)}]^T$$

$$\mathbf{C} = \begin{bmatrix} 1/2 - a_A & 1/2 - a_B & -a_C & -a_D & -a_E \\ -a_A & -a_B & 1/2 - a_C & 1/2 - a_D & -a_E \\ 0 & 0 & 0 & 0 & 1 \\ 1/2 & -1/2 & 0 & 0 & 0 \\ 0 & 0 & 1/2 & -1/2 & 0 \\ a_A & a_B & a_C & a_D & a_E \end{bmatrix}. \quad (26)$$

To couple the membrane strains with the bending and transverse shear strains of the MITC4+ shell element, the assumed membrane strain \tilde{e}_{ij} in Eq. (14) is transformed into the covariant coordinate system using $\tilde{e}_{ij} = (\mathbf{g}_i \cdot \hat{\mathbf{g}}^k)(\mathbf{g}_j \cdot \hat{\mathbf{g}}^l)\tilde{e}_{kl}$ [1,12,13]. This transformation can be denoted by the following relations,

$$\begin{bmatrix} \tilde{e}_{rr} \\ \tilde{e}_{ss} \\ \tilde{e}_{rs} \end{bmatrix} = \mathbf{T}(r, s) \begin{bmatrix} \tilde{e}_{rr} \\ \tilde{e}_{ss} \end{bmatrix} + \mathbf{S}(r, s)\tilde{e}_{rs}$$

with

$$\mathbf{T}(r, s) = \begin{bmatrix} (1 + c_r s)^2 & (c_s s)^2 \\ (c_r r)^2 & (1 + c_s r)^2 \\ c_r r(1 + c_r s) & c_s s(1 + c_s r) \end{bmatrix}, \quad (27)$$

$$\mathbf{S}(r, s) = \begin{bmatrix} 2c_s s(1 + c_r s) \\ 2c_r r(1 + c_s r) \\ c_r c_s r s + (1 + c_r s)(1 + c_s r) \end{bmatrix},$$

where the entries are derived from

$$\begin{aligned} \mathbf{g}_s \cdot \hat{\mathbf{g}}^r &= (\mathbf{g}_s + r\mathbf{x}_d) \cdot \hat{\mathbf{g}}^r = c_r r, & \mathbf{g}_r \cdot \hat{\mathbf{g}}^s &= (\mathbf{g}_r + s\mathbf{x}_d) \cdot \hat{\mathbf{g}}^s = c_s s, \\ \mathbf{g}_r \cdot \hat{\mathbf{g}}^r &= (\mathbf{g}_r + s\mathbf{x}_d) \cdot \hat{\mathbf{g}}^r = 1 + c_r s, & \mathbf{g}_s \cdot \hat{\mathbf{g}}^s &= (\mathbf{g}_s + r\mathbf{x}_d) \cdot \hat{\mathbf{g}}^s = 1 + c_s r. \end{aligned} \quad (28)$$

Combining Eqs. (20), (26) and (27), the final form of the assumed membrane strain is given by

$$\begin{bmatrix} \tilde{e}_{rr} \\ \tilde{e}_{ss} \\ \tilde{e}_{rs} \end{bmatrix} = \mathbf{A}(r, s)\mathbf{C} [e_{rr}^{(A)} \quad e_{rr}^{(B)} \quad e_{ss}^{(C)} \quad e_{ss}^{(D)} \quad e_{rs}^{(E)}]^T + \mathbf{S}(r, s)e_{rs}^{(E)}, \quad (29)$$

in which $\mathbf{A}(r, s) = \mathbf{T}(r, s)\mathbf{M}^T(r, s)$. Note that the matrices $\mathbf{M}(r, s)$, $\mathbf{T}(r, s)$ and $\mathbf{S}(r, s)$ given in Eqs. (20) and (27) are functions of r and s , while the matrix \mathbf{C} defined in Eq. (26) is constant.

Note that in Eq. (29) the strain-displacement matrices for the tying strains ($e_{rr}^{(A)}$, $e_{rr}^{(B)}$, $e_{ss}^{(C)}$, $e_{ss}^{(D)}$ and $e_{rs}^{(E)}$) and the matrix \mathbf{C} can be pre-calculated for each element. The computations needed at each Gauss integration point are reduced to the calculation of small-sized matrices ($\mathbf{A}(r, s)$ and $\mathbf{S}(r, s)$). The element is referred to as an “improved MITC4+ shell element”.

Note that in this element formulation we do not use the assumption of a constant volumetric strain over the element. Therefore, as mentioned above already, when this shell element is used in a (planar) plane stress solution, the results will be the same as when using the 2D-MITC4 element.

All 4-node elements considered in this study are integrated using 2×2 Gauss integration in the $r-s$ plane, while for the shell element, also 2-point Gauss integration is employed in the thickness direction.

4. Basic numerical tests

The formulations of the 2D-MITC4 and improved MITC4+ elements do not use any numerical factor or internal degrees of freedom. We consider here the isotropy, zero energy mode and patch tests. When we refer here to the 2D-MITC4 element, we also include the 2D-MITC4/1 element.

The spatially isotropic behavior is an important consideration for any element. The element behavior should not depend on the sequence of node numbering [1,14,15]. The 2D-MITC4 and improved MITC4+ elements pass the isotropy test.

In the zero energy mode test, the stiffness matrix of a single unsupported element should show only zero eigenvalues corresponding to the correct rigid body modes. Three rigid body modes (2 translations and 1 rotation) and six rigid body modes (3 translations and 3 rotations) should be present for 2D solid and shell elements, respectively. Both the 2D-MITC4 and improved MITC4+ elements pass this test.

In the patch tests [1], the patch of elements shown in Fig. 7 is subjected to the minimum number of constraints to prevent rigid body motions, and forces are applied at the boundary corresponding to the constant stress states. The predicted stresses should then be the analytically correct values of stresses at any location in the patch. The 2D-MITC4 and improved MITC4+ elements pass the membrane patch tests, and the improved MITC4+ shell element additionally passes the bending and shearing patch tests.

5. Illustrative solutions for 2D-solid problems

In this section, we present the performance of the new 2D solid elements through the solutions of well-known 2D examples established to check in-plane shear locking and volumetric locking. Comparisons are made with the standard displacement based 4-node element referred to as “Q4” as well as the standard 4-node incompatible modes element referred to as “Q4I4”, see Refs. [1,6,7].

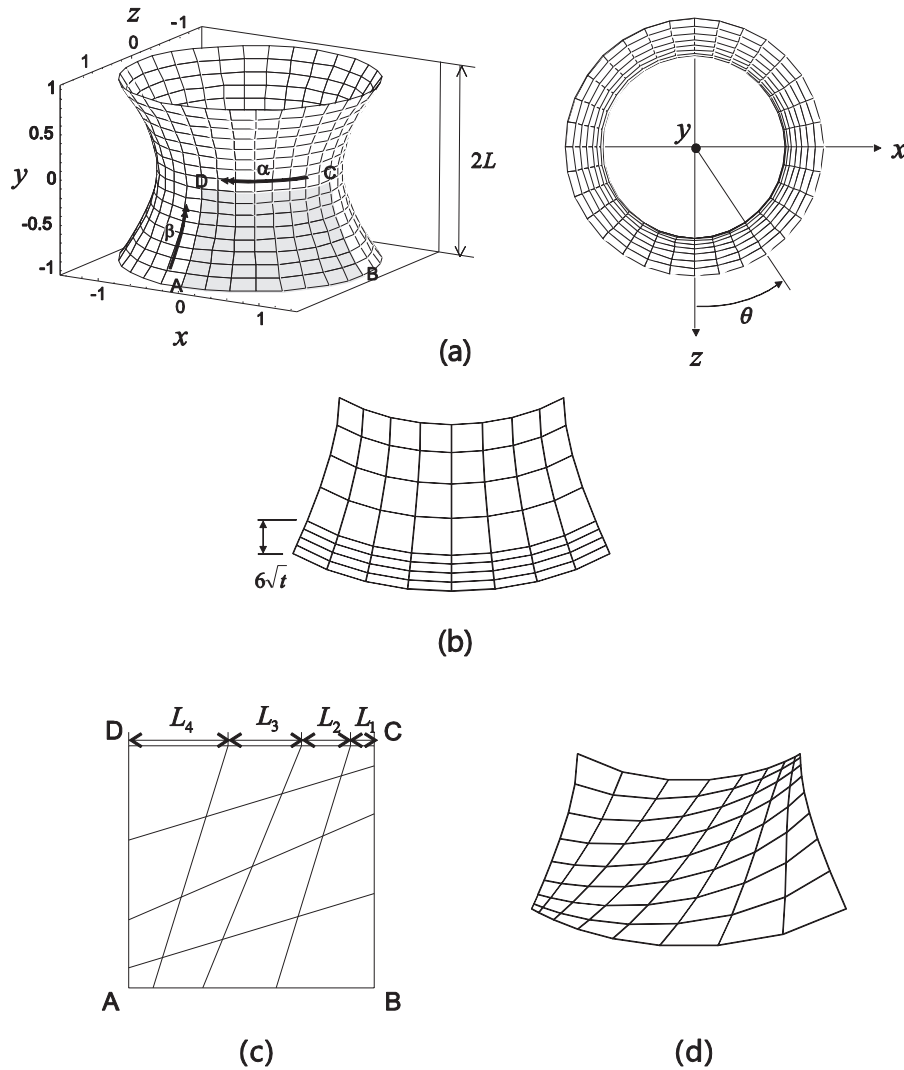


Fig. 20. Hyperboloid shell problem ($E = 2.0 \times 10^{11}$, $\nu = 1/3$, $L = 1.0$ and $p_0 = 1.0$). (a) Problem description. (b) Graded regular mesh (8×8 mesh, $t/L = 1/1000$). (c) Distorted mesh pattern (4×4 element mesh). (d) Used distorted mesh (8×8 element mesh).

The performance of the new solid elements is investigated in linear plane stress and strain analyses, namely, a cantilever beam problem, a curved beam problem, Cook's problem and a clamped square plate subjected to an in-plane moment. We also include geometrically nonlinear analyses to see whether a possible instability arises that may be seen using an EAS element [4,8–11]. To use the incompatible modes element in nonlinear analysis, we employ ADINA [25]. For the 2D-MITC4 element, we implemented the classical total Lagrangian formulation [1].

5.1. Cantilever problem

We solve the cantilever problem shown in Fig. 8. The structure is subjected to a shearing force at its tip. The cantilever is modeled using regular and distorted meshes with four elements as in Refs. [26–28].

Tables 1 and 2 give the tip vertical displacement at point A and the xx -component of stress at point B, respectively, with reference to the reference solutions. The use of the 2D-MITC4 and 2D-MITC4/1 elements gives the exact values for the regular mesh as does the Q4I4 element. For the distorted mesh case, the solutions using the 2D-MITC4 and 2D-MITC4/1 elements are much more accurate than when using the standard displacement-based ele-

ment and the 2D-MITC4/1 element gives solutions not much less accurate than obtained using the Q4I4 element.

5.2. Curved beam problem

We next consider the curved beam problem in Fig. 9 [27,28]. The curved beam is subjected to a shearing force of total magnitude P at its tip; plane stress conditions are assumed. We use meshes of $N \times 4N$ elements, $4N$ elements along the beam length, with $N = 1, 2, 4$ and 8 . Through this problem, we test the predictive capability of the elements in a mixed behavior of bending and shearing when naturally distorted meshes are used.

Tables 3 and 4 give the predicted tip vertical displacement at point A and the yy -component of stress at the support point B, respectively. The reference solutions for the displacement and stress are obtained from the solution using a 16×64 mesh of 9-node displacement-based elements.

The predictions in displacement and stress using the 2D-MITC4 and Q4I4 elements are not far apart.

5.3. Cook's problem

We consider the well-known Cook's problem [6,22,26] shown in Fig. 10. The cantilever is clamped at one end and is subjected to a

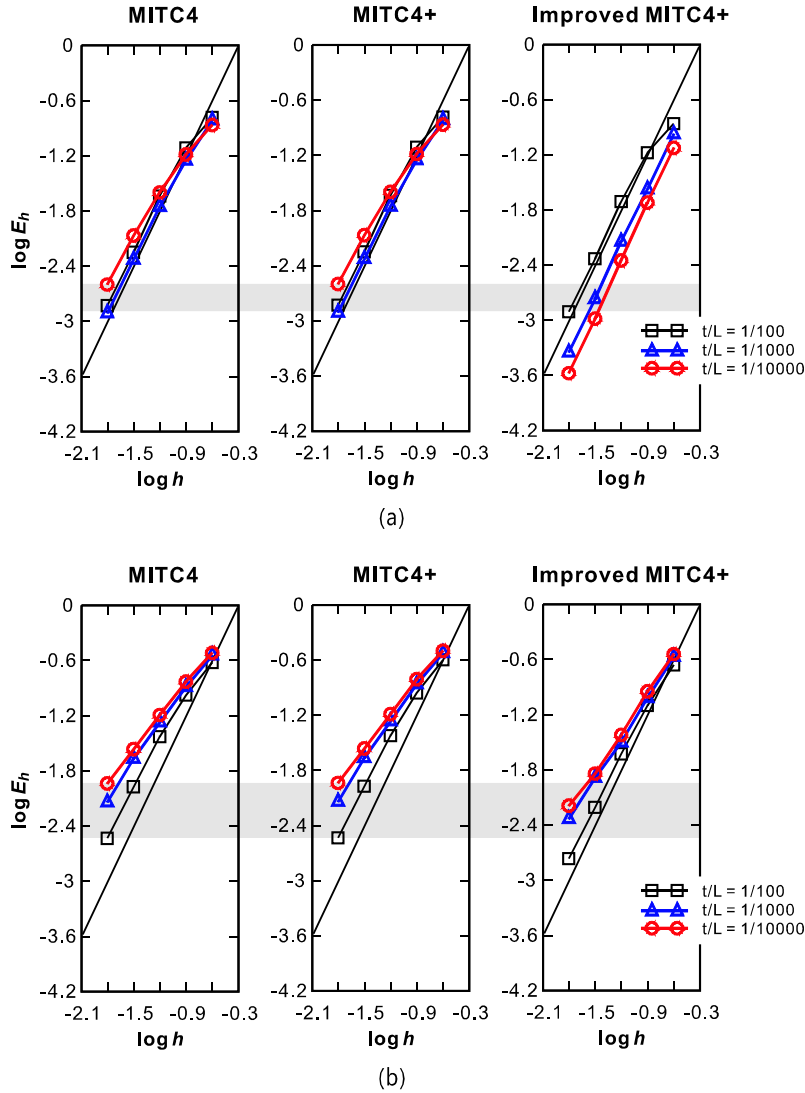


Fig. 21. Convergence curves for the clamped hyperboloid shell problem with (a) the graded regular and (b) distorted meshes. The bold line represents the optimal convergence rate.

distributed shearing force of total magnitude P at its tip. We consider the solutions using plane stress conditions with Poisson's ratio $\nu = 1/3$, plane strain conditions with $\nu = 0.3, 0.4$ and 0.499 , and meshes of $N \times N$ elements with $N = 2, 4, 8, 16$ and 32 . The regions of stress singularities at the top and bottom of the clamped boundary are very small and do not affect the overall results.

Table 5 gives the vertical displacement at point A for the plane stress case. The performance of the 2D-MITC4 element is similar to that of the Q4I4 element. For the plane strain case, we measure the solution error using the s-norm [16,19] with reference solutions obtained using a 72×72 mesh of the standard 9-node displacement-based element (Q9) for the cases $\nu = 0.3, 0.4$ and the 9/3 element for the case $\nu = 0.499$ [1],

$$\|\mathbf{u}_{ref} - \mathbf{u}_h\|_s^2 = \int_{\Omega_{ref}} \Delta \boldsymbol{\varepsilon}^T \Delta \boldsymbol{\tau} d\Omega_{ref} \quad \text{with} \quad \Delta \boldsymbol{\varepsilon} = \boldsymbol{\varepsilon}_{ref} - \boldsymbol{\varepsilon}_h, \quad \Delta \boldsymbol{\tau} = \boldsymbol{\tau}_{ref} - \boldsymbol{\tau}_h,$$

$$E_h = \frac{\|\mathbf{u}_{ref} - \mathbf{u}_h\|_s^2}{\|\mathbf{u}_{ref}\|_s^2}, \quad (30)$$

where \mathbf{u}_{ref} is the reference solution, \mathbf{u}_h is the solution of the finite element discretization, and $\boldsymbol{\varepsilon}$ and $\boldsymbol{\tau}$ are the strain and stress vectors, and E_h is the relative error.

The optimal convergence for 4-node bilinear elements is given by

$$E_h \cong Ch^2, \quad (31)$$

in which C is a constant independent of the material properties and h is the element size.

Fig. 11 shows the convergence of the relative error according to the element size $h = 1/N$. While the Q4 element severely locks near the incompressible limit, the convergence of the 2D-MITC4/1 and Q4I4 elements is nearly optimal regardless of Poisson's ratio.

5.4. Clamped square plate subjected to an in-plane moment

We solve a clamped square plate subjected to an in-plane moment of magnitude M , see Fig. 12. We assume plane strain conditions with Poisson's ratios $\nu = 0.3, 0.4$ and 0.499 . For the solutions we use regular and distorted meshes with $N \times N$ elements and $N = 2, 4, 8, 16$ and 32 , see Fig. 12(a), and (b), where the element edges are discretized in the ratio $L_1 : L_2 : L_3 : \dots : L_N = 1 : 2 : 3 : \dots : N$. The regions of stress singularities at the top and bottom of the clamped boundary are very small and do not affect the overall results.

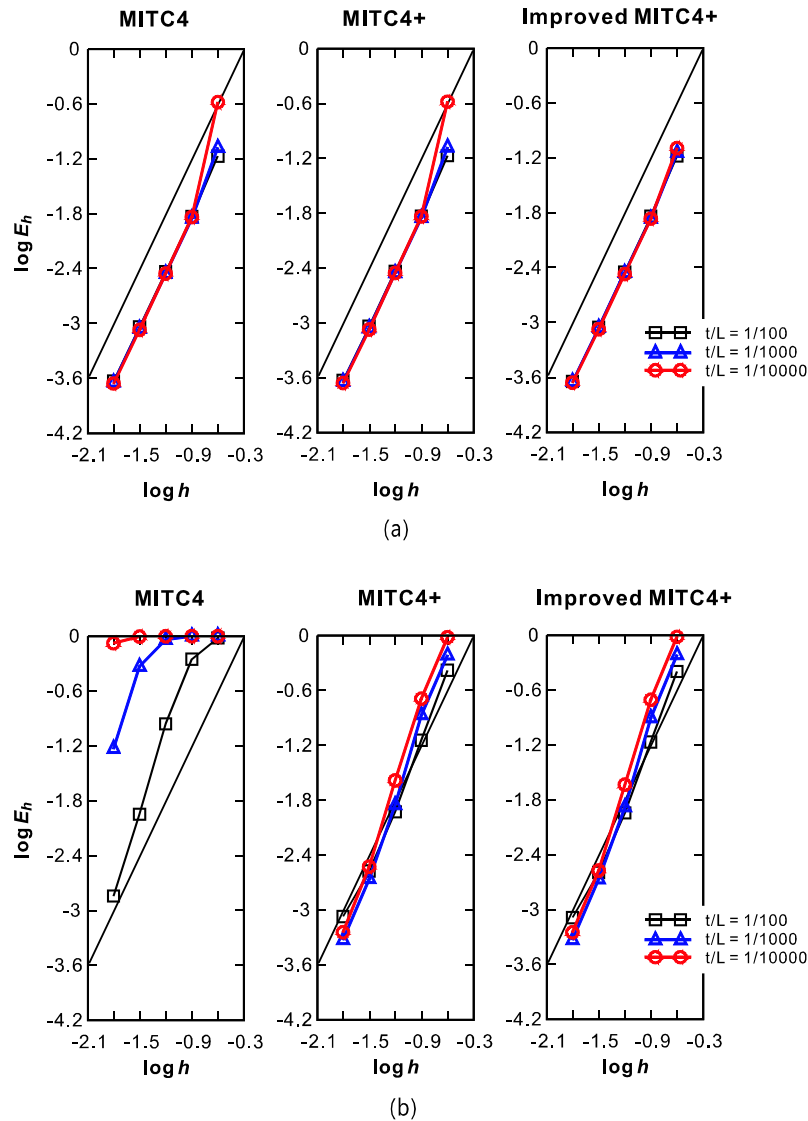


Fig. 22. Convergence curves for the free hyperboloid shell problem with (a) the graded regular and (b) distorted meshes. The bold line represents the optimal convergence rate.

The relative error is measured using the s-norm with the reference solutions obtained using a 72×72 mesh of the standard 9-node displacement-based element (Q9) for the cases $\nu = 0.3, 0.4$ and the 9/3 element for the case $\nu = 0.499$. Fig. 13 shows that the 2D-MITC4/1 element converges optimally in both the uniform and distorted mesh cases irrespective of Poisson's ratio.

5.5. Rubber block problem

We solve the geometrically nonlinear problem of a rubber block subjected to compression as shown in Fig. 14 [9,10]. Solving this problem, we want to investigate whether our new element shows spurious modes as seen when using the incompatible modes (EAS) element. [4,8–11]. The distributed load with a force per unit length P is asymmetrically applied to the rubber block.

Fig. 15 shows the load-displacement curves with the reference solution obtained using the standard 9-node displacement-based element (Q9) because Poisson's ratio is not close to 0.5. The meshes are not fine and so we do not claim to have reached a close approximation to the exact solution. Unlike the Q4 element showing a too stiff behavior, the Q4I4 and 2D-MITC4/1 elements closely follow

the reference load-displacement path. However, when the Q4I4 element is employed, the analysis predicts an instability at $P = 80.4$, which is spurious. This phenomenon is well-known and can even happen at very small strain levels [11]. The deformed shape shown in Fig. 16 reveals the spurious hour-glassing encountered [4,8–11]. The 2D-MITC4/1 element does not show any spurious instability.

5.6. Composite block problem

We consider next the geometrically nonlinear compression of the composite block shown in Fig. 17. While the base material is the same as in the previous problem, a stiff material with low Poisson's ratio is used in the shaded region. We want to study the behavior of the 4-node EAS element under high compressive strains. The block is fully clamped at the bottom and the distributed load with force per unit length P is applied.

Fig. 18 shows the predicted load-displacement curves with the reference solution obtained using the Q9 element because Poisson's ratio is not close to 0.5. While the solution using the 2D-MITC4 element closely follows the reference load-displacement

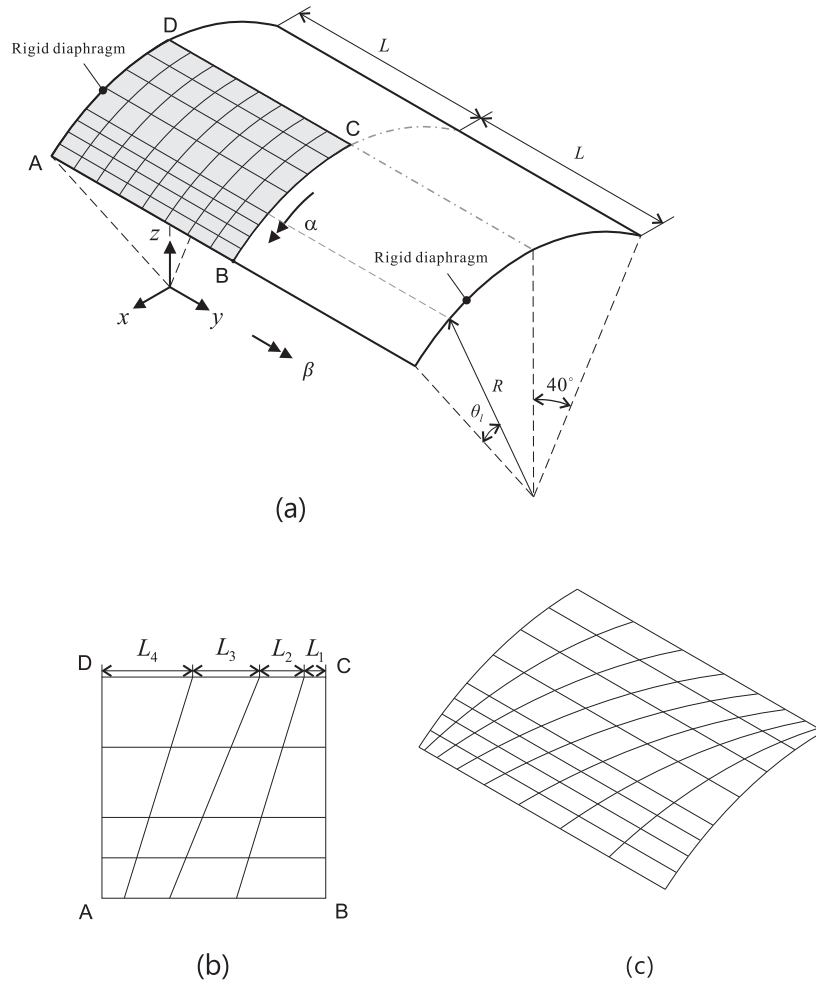


Fig. 23. Scordelis-Lo roof shell problem ($E = 4.32 \times 10^8$, $\nu = 0.0$, $R = 25.0$, $L = 25.0$ and self-weight is 90 per unit surface area). (a) Problem description with graded regular mesh (8×8 element mesh). (b) Distorted mesh pattern (4×4 element mesh). (c) Used distorted mesh (8×8 element mesh).

curve, the solution obtained using the Q4I4 element does not follow the reference solution and predicts a spurious collapse load. The deformations are compared in Fig. 19. For the EAS element, strong element hourglass-shapes are observed. However, the geometric predictions obtained using the 2D-MITC4/1 element are smooth as in the reference solution.

6. Illustrative solutions of shell problems

In this section, we present the performance of the improved MITC4+ shell element, in which the in-plane membrane field of the 2D-MITC4 solid element is used. The hyperboloid shell problems and the Scordelis-Lo roof problems are considered [12,14–19,29]. We vary the ratio of the shell thickness to the overall dimension of the structure, $t/L = 1/100$, $1/1000$ and $1/10,000$. The convergence of the finite element solutions is measured using the s-norm in Eq. (30). The results of the improved MITC4+ shell element are compared with those using the MITC4 [13] and MITC4+ [12] shell elements.

6.1. Hyperboloid shell problems

The hyperboloid shell shown in Fig. 20(a) is considered, see Refs. [12,14–19]. The mid-surface of the shell structure is given by

$$x^2 + z^2 = 1 + y^2; \quad y \in [-1, 1]. \quad (32)$$

The loading is a smoothly varying pressure $p(\theta)$

$$p(\theta) = p_0 \cos(2\theta). \quad (33)$$

Due to symmetry, only one-eighth of the structure corresponding to the shaded region ABCD in Fig. 20(a) is modeled for the analysis. For the membrane-dominated case, the clamped boundary condition is imposed: $u_z = \beta = 0$ along BC, $u_x = \beta = 0$ along AD, $u_y = \alpha = 0$ along DC, and $u_x = u_y = u_z = \alpha = \beta = 0$ along AB. For the bending-dominated case, the free boundary condition is imposed: $u_z = \beta = 0$ along BC, $u_x = \beta = 0$ along AD, and $u_y = \alpha = 0$ along DC.

The solutions are calculated using $N \times N$ element meshes ($N = 4, 8, 16, 32$ and 64). The element size is $h = L/N$. For the clamped (free) boundary condition, the regular mesh is graded as shown in Fig. 20(b) in a boundary layer of width $6\sqrt{t}$ ($0.5\sqrt{t}$), see Refs. [12,14–19]. We also perform the convergence studies with the distorted mesh pattern shown in Fig. 20(c), where each edge is discretized in the following ratio: $L_1 : L_2 : L_3 : \dots : L_N = 1 : 2 : 3 : \dots : N$ for the $N \times N$ element mesh. The applied distorted mesh is shown in Fig. 20(d). A 72×72 element mesh of MITC9 shell elements [17–19] is used to obtain the reference solutions

Fig. 21 shows that the improved MITC4+ shell element performs noticeably better than the MITC4+ shell element for all shell problems. As reported earlier, when using the MITC4 element in the distorted meshes, the results severely deteriorate due to membrane locking, see Fig. 22.

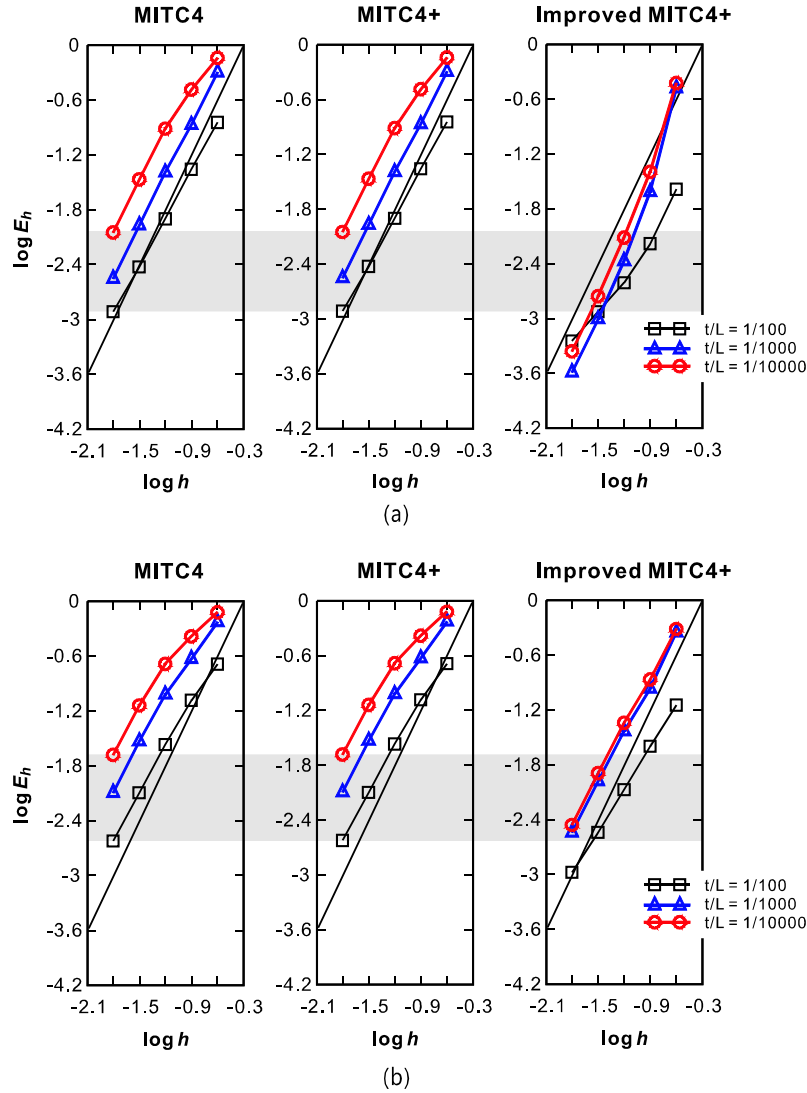


Fig. 24. Convergence curves for the Scordelis-Lo roof shell problem with (a) the regular meshes (b) distorted meshes. The bold line represents the optimal convergence rate.

6.2. Scordelis-Lo roof shell problem

The Scordelis-Lo roof shell problem shown in Fig. 23(a) is considered [13,18,19,29]. The 40° roof structure with radius R and length $2L$ is supported by rigid diaphragms. The structure is loaded by its self-weight. The structure is known to asymptotically show membrane-bending mixed behavior [18,19].

Utilizing the symmetry, only one-quarter of the structure corresponding to the shaded region ABCD in Fig. 23(a) is modeled for the analysis. The following boundary condition is imposed: $u_x = \beta = 0$ along DC, $u_y = \alpha = 0$ along BC, and $u_x = u_z = \beta = 0$ along AD. As the thickness becomes small, the mesh is graded according to the following layer angle formula applied for $\theta_l < 40^\circ$ [18]

$$\theta_l = 5.35L^{0.75}t^{0.25}. \quad (34)$$

Fig. 23(a) shows a regular mesh with the mesh grading. We also perform the convergence studies with distorted meshes, see Fig. 23(b). Here, mesh grading along the edges BC and AD is still used, but the edges AB and CD are discretized in the following ratio: $L_1: L_2: L_3: \dots: L_N = 1: 2: 3: \dots: N$ for the $N \times N$ element mesh.

Fig. 24 shows the predicted convergence curves. The solutions are obtained with $N \times N$ element meshes ($N = 4, 8, 16, 32$, and 64). The reference solutions are calculated using a 72×72 element

mesh of MITC9 shell elements. When compared with the MITC4 and the MITC4+ shell elements, the improved MITC4+ shell element shows improvements in solution accuracy.

7. Concluding remarks

A new 2D-MITC4 element was presented for the two-dimensional analysis of problems in solid mechanics. The 2D-MITC4 element passes all basic tests and performs well in linear analyses, almost as well as the 4-node incompatible modes (EAS) element. In the geometrically nonlinear problems solved, the new element also performs well and does not show a spurious instability, as observed with the EAS element. The 2D-MITC4 element is computationally effective because no degrees-of-freedom other than those for the 4-node displacement-based element are used. While we considered only plane stress and plane strain conditions, the element formulation can be extended for axisymmetric analyses, and while we considered only static analyses, the element will also be valuable in dynamic solutions because the mass matrix is formulated as for the pure displacement-based element.

Using the 2D-MITC4 formulation for the membrane strain of the MITC4+ shell element, we further improved the performance of

this shell element, although not very much, because the MITC4+ element is already close to optimal.

For plane strain analyses, and in particular almost incompressible media, we formulated the 2D-MITC4/1 element assuming a constant pressure. This element also passes all basic tests. The element can as well be used in plane stress analyses and may yield more accurate results than the 2D-MITC4 element. A mathematical analysis of both elements would be valuable.

This paper also demonstrates once more that the MITC method is not only valuable to formulate plate and shell elements but indeed may also give more powerful elements for the simulation of solids and multiphysics problems [30–32].

Acknowledgments

This research was supported by a grant (MPSS-CG-2016-04) through the Disaster and Safety Management Institute funded by Ministry of Public Safety and Security of Korean government, and the Climate Change Research Hub of KAIST (No. 11170061).

References

- [1] Bathe KJ. Finite element procedures. Prentice Hall; 1996, 2nd ed. KJ. Bathe, Watertown, MA; 2014 and Higher Education Press, China; 2016.
- [2] Bathe KJ. The inf-sup condition and its evaluation for mixed finite element methods. *Comput Struct* 2001;79(2):243–52.
- [3] Pantuso D, Bathe KJ. A four-node quadrilateral mixed-interpolated element for solids and fluids. *Math Models Methods Appl Sci* 1995;5(8):1113–28.
- [4] Pantuso D, Bathe KJ. On the stability of mixed finite elements in large strain analysis of incompressible solids. *Finit Elem Anal Des* 1997;28(2):83–104.
- [5] Wilson EL, Taylor RL, Doherty WP, Ghaboussi J. Incompatible displacement models: numerical and computer methods in structural mechanics. New York: Academic Press; 1973. p. 43–57.
- [6] Simo JC, Rifai MS. A class of mixed assumed strain methods and the method of incompatible modes. *Inter J Numer Meth Eng* 1990;29(8):1595–638.
- [7] Wilson EL, Ibrahimbegovic A. Use of incompatible displacement modes for the calculation of element stiffnesses or stresses. *Finit Elem Anal Des* 1990;7(3):229–41.
- [8] Wriggers P, Reese S. A note on enhanced strain methods for large deformations. *Comp Meth Appl Mech Eng* 1996;135:201–9.
- [9] Wall WA, Bischoff M, Ramm E. A deformation dependent stabilization technique, exemplified by EAS elements at large strains. *Comp Meth Appl Mech Eng* 2000;188(4):859–71.
- [10] Bischoff M, Bletzinger KU. Interaction of locking and element stability at large strains. In: VIII International conference on computational plasticity, Barcelona; 2005.
- [11] Sussman T, Bathe KJ. Spurious modes in geometrically nonlinear small displacement finite elements with incompatible modes. *Comput Struct* 2014;140:14–22.
- [12] Ko Y, Lee PS, Bathe KJ. A new MITC4+ shell element. *Comput Struct* 2017;182:404–18.
- [13] Dvorkin EN, Bathe KJ. A continuum mechanics based four-node shell element for general nonlinear analysis. *Eng Comput* 1984;1(1):77–88.
- [14] Lee PS, Bathe KJ. Development of MITC isotropic triangular shell finite elements. *Comput Struct* 2004;82(11):945–62.
- [15] Lee Y, Lee PS, Bathe KJ. The MITC3+ shell element and its performance. *Comput Struct* 2014;138:12–23.
- [16] Hiller JF, Bathe KJ. Measuring convergence of mixed finite element discretizations: an application to shell structures. *Comput Struct* 2003;81(8):639–54.
- [17] Bathe KJ, Lee PS, Hiller JF. Towards improving the MITC9 shell element. *Comput Struct* 2003;81(8):477–89.
- [18] Lee PS, Bathe KJ. On the asymptotic behavior of shell structures and the evaluation in finite element solutions. *Comput Struct* 2002;80(3):235–55.
- [19] Chapelle D, Bathe KJ. The finite element analysis of shells – fundamentals. 1st ed. Springer; 2003. 2nd ed., Springer, 2011.
- [20] Bucalem ML, Bathe KJ. The mechanics of solids and structures – hierarchical modeling and the finite element solution. Springer; 2011.
- [21] Sussman T, Bathe KJ. A finite element formulation for nonlinear incompressible elastic and inelastic analysis. *Comput Struct* 1987;26(1–2):357–409.
- [22] Dvorkin EN, Vassolo SI. A quadrilateral 2-D finite element based on mixed interpolation of tensorial components. *Eng Comput* 1989;6(3):217–24.
- [23] Choi CK, Paik JG. An efficient four node degenerated shell element based on the assumed covariant strain. *Struct Eng Mech* 1994;2(1):17–34.
- [24] Roh HY, Cho M. The application of geometrically exact shell elements to B-spline surfaces. *Comp Meth Appl Mech Eng* 2004;193(23):2261–99.
- [25] <http://www.adina.com/>.
- [26] Chen XM, Cen S, Long YQ, Yao ZH. Membrane elements insensitive to distortion using the quadrilateral area coordinate method. *Comput Struct* 2004;82(1):35–54.
- [27] Cen S, Chen XM, Fu XR. Quadrilateral membrane element family formulated by the quadrilateral area coordinate method. *Comp Meth Appl Mech Eng* 2007;196(41):4337–53.
- [28] Long ZF, Cen S, Wang L, Fu XR, Long YQ. The third form of the quadrilateral area coordinate method (QACM-III): theory, application, and scheme of composite coordinate interpolation. *Fin Elem Anal Design* 2010;46(10):805–18.
- [29] Scordelis AC, Lo KS. Computer analysis of cylindrical shells. *J Am Concr Inst* 1969;61(5):539–62.
- [30] Bathe KJ. Advances in the Multiphysics Analysis of Structures. In: Topping BHV, editor. Chapter 1 in computational methods for engineering science. Saxe-Coburg Publications, Stirlingshire, Scotland; 2012.
- [31] Bathe KJ. Frontiers in finite element procedures & applications. In: Topping BHV, Iványi P, editors. Chapter 1 in computational methods for engineering technology. Saxe-Coburg Publications, Stirlingshire, Scotland; 2014.
- [32] Bathe KJ, Zhang H, Yan Y. The solution of Maxwell's equations in multiphysics. *Comput Struct* 2014;132:99–112.